

$b]/2, [a + b]/2, c/2$). These four surfaces are mapped onto another, for example, by the symmetry operations listed in Table 1.

The genus is 9 for *MC6* as well as for *MC7* surfaces.

7. Minimal surfaces *oMC5* (double catenoids)

Rectangular nets 4^4 of twofold axes (case 26) are defined by orthorhombic group-subgroup pairs of 33 types. Only 12 of them are compatible with catenoid-like surface patches and with the respective minimal balance surfaces *oP*, a family of orthorhombically distorted *P* surfaces.

Quite similarly as described above for *MC5* surfaces, the fusion of two such catenoids results in a double catenoid, a surface patch of an *oMC5* surface. The surfaces of the family *oMC5* may be regarded as orthorhombically distorted *MC5* surfaces. The family *oMC5* comprises the surfaces of the family *MC5* as a limiting case ($a = b$).

oMC5 surfaces are compatible with group-subgroup pairs of only two of the 12 types mentioned above: *Pccm-P2/m* and *P222-P2*. The inherent symmetry of *oMC5* surfaces is *Pccm-P2/m*.

Analogously to *MC5* surfaces each set of rectangular nets of twofold axes may generate eight congruent *oMC5* surfaces; but in contrast to *MC5* surfaces all these *oMC5* surfaces have identical inherent symmetry. They can be mapped onto another by symmetry operations of the intersection group $N_E(Pccm) \cap N_E(P2/m) = Pmmm(a/2, b/2, c/2)$ (cf. Table 1).

8. Common properties of *MC* surfaces

For all minimal balance surfaces built up from multiple catenoids two layers of such catenoids exist per *c*-translation period. The central axes of the multiple catenoids are the same for the catenoids of different

layers. Multiple catenoids from different layers with the same central axis are oriented differently.

If the generating linear net of an *MC* surface consists of triangular nets of twofold axes six *MC* surfaces exist which are complementary to each other. In the case of quadrangular nets eight complementary *MC* surfaces occur. Each vertex of a triangle or a quadrangle corresponds to two congruent *MC* surfaces. Equivalent vertices give rise to congruent surfaces, non-equivalent ones to non-congruent surfaces. Each of these surfaces is complementary in addition to two congruent minimal surfaces built up from catenoids (except *MC5* surfaces with $a = 2^{1/2}c$ and *oMC5* surfaces with $a = b = 2^{1/2}c$). The use of the capital letter *C* for the designation of complicated new minimal surfaces which are complementary to known ones is therefore misleading [cf. Schoen (1970): *C(H), C(P), C(D)*; Fischer & Koch (1987): *C(S), C(Y) etc.*], and should be avoided in the future.

Minimal surfaces with multiple catenoids as surface patches exist only within a certain range of the axial ratio $0 < c/a \leq c/a(\text{max.})$. As for minimal surfaces consisting of catenoids or branched catenoids the upper limits $c/a(\text{max.})$ are unknown. It has been shown by soap-film experiments that multiple catenoids allow a larger distance between neighbouring nets of twofold axes than the corresponding simple catenoids.

References

- FISCHER, W. & KOCH, E. (1987). *Z. Kristallogr.* **179**, 31-52.
 FISCHER, W. & KOCH, E. (1989). *Acta Cryst.* **A45**, 166-169.
 HYDE, S. T. & ANDERSSON, ST. (1984). *Z. Kristallogr.* **168**, 221-254.
 KOCH, E. & FISCHER, W. (1988). *Z. Kristallogr.* In the press.
 SCHOEN, A. H. (1970). *Infinite Periodic Minimal Surfaces Without Self-Intersections*. NASA Tech. Note No. D-5541.
 SCHWARZ, H. A. (1890). *Gesammelte mathematische Abhandlungen*, Band 1. Berlin: Springer.

Acta Cryst. (1989). **A45**, 174-182

Bloch-Wave Solution in the Bragg Case

BY Y. MA AND L. D. MARKS

Department of Materials Science, Northwestern University, Evanston, IL 60208, USA

(Received 4 January 1988; accepted 16 September 1988)

Abstract

The Bloch-wave method for reflection diffraction problems, primarily electron diffraction as in reflection high-energy electron diffraction (RHEED) and reflection electron microscopy (REM), is developed.

The basic Bloch-wave approach for surfaces is reviewed, introducing the current flow concept which plays a major role both in understanding reflection diffraction and determining the allowed Bloch waves. This is followed by a brief description of the numerical methods for obtaining the results including

specific results for GaAs near to the [010] zone axis. A number of other Bloch-wave phenomena are also discussed, namely resonance diffraction and its relationship to internal and external reflection and variations in the boundary conditions and Bloch-wave character, splitting of diffraction spots due to stepped surfaces, which can be completely explained, and the reflection equivalent of thickness fringes.

1. Introduction

It is well known that reflection high-energy electron diffraction (RHEED) and reflection electron microscopy (REM) are powerful tools for investigating surface structure. As Menadue (1972) pointed out, it is not unreasonable to expect that some of the techniques developed for transmission electron diffraction and imaging can be extended to study and understand the structures of crystal surfaces. Although techniques for understanding reflection diffraction of electrons based upon modified low-energy electron diffraction (LEED) programs have been developed by a number of authors (*e.g.* Colella & Menadue, 1972; Moon, 1972; Maksym & Beeby, 1981), and Bloch-wave approaches using slices perpendicular to the surface (*e.g.* Schuman, 1977) and a method based upon the multislice approach by Peng & Cowley (1986) have been discussed, a complete understanding has yet to be attained. For instance, it is not clear that any of the modified LEED approaches can be used for surface defects. Most of the Bloch-wave approaches have only used simplified systematic conditions and the multislice approach uses a top-hat incident wave with smooth edges to model an incident plane wave and as such suffers from problems in attaining a static solution and edge effects from the sides of the top-hat incident wave.

In principle, a very powerful method for understanding electron diffraction is the Bloch-wave method which was used widely in understanding diffraction from perfect and imperfect crystals. One of the main advantages of the Bloch-wave method is that it allows access to analytical methods which can lead to substantial physical insights which are often not readily available in strictly numerical methods, and there are numerous methods based on Bloch waves which, for instance, can be used as methods for calculating the image contrast from surface defects (*e.g.* Schuman, 1977). In addition, for thicker crystals, as is the case for Bragg diffraction, it can be much faster than numerical methods such as multislice.

This paper will give a detailed description of both the analytical theory and numerical solutions of the Bloch-wave approach in the Bragg case, in part recapping some of the earlier development of workers such as Metherell (1972), and in part developing new work particularly on the boundary value problem and the splitting of diffraction spots due to surface steps.

Whilst many workers have tackled this problem using simplified Bloch-wave models and systematic orientations, we have here developed the method for more complicated many-beam conditions which more closely resemble experimental conditions. In the process of this analysis we also bring out the importance of reflectivity *via* the current flow in terms of understanding the physics of reflection. Based upon this approach we then briefly discuss dynamical explanations of surface resonance, spot splitting due to surface steps and the reflection analogy of thickness fringes. A more detailed analysis of spot splitting due to surface steps (Marks & Ma, 1988*b*) and a combination of Bloch and multislice approaches to rigorous calculations of surface defect scattering (Ma & Marks, 1989) will be presented elsewhere.

2. Bloch formulation in a general case

The general theory of dynamical electron diffraction in a crystal was first proposed by Bethe (1928), and a systematic review of the theory can be found in the paper by Metherell (1972). We will briefly recap this primarily to define our notation. In a periodic potential field, the electron wave has the form of a Bloch wave, which can be expanded as the Fourier series

$$\psi^j(\mathbf{r}) = \sum_{\mathbf{g}} C_{\mathbf{g}}^j \exp[2\pi i(\mathbf{k}^j + \mathbf{g}) \cdot \mathbf{r}] \quad (1)$$

where $C_{\mathbf{g}}^j$ and $\mathbf{k}^j + \mathbf{g}$ are the coefficients and the wave vectors of the plane-wave components and j indexes the Bloch wave. Substituting the Bloch-wave form into Schrödinger's equation and using a Fourier expansion of the crystal potential $V(r)$, we obtain

$$\sum_{\mathbf{g}} \{(1 - \delta_{\mathbf{g}\mathbf{h}})U_{\mathbf{g}-\mathbf{h}} + \delta_{\mathbf{g}\mathbf{h}}[K^2 - (\mathbf{k}^j + \mathbf{g})^2]\} C_{\mathbf{g}}^j = 0 \quad (2)$$

where $K = 2meE/\hbar^2 + U_c$ and $U_{\mathbf{g}} = 2meV_{\mathbf{g}}/\hbar^2$. Equation (2) can also be written in matrix form as

$$\begin{vmatrix} K^2 - (\mathbf{k}^j + \mathbf{g})^2 & U_{\mathbf{g}-\mathbf{h}} & \dots \\ U_{\mathbf{h}-\mathbf{g}} & K^2 - (\mathbf{k}^j + \mathbf{h})^2 & \dots \\ \dots & \dots & K^2 - (\mathbf{k}^j + \mathbf{l})^2 \end{vmatrix} \begin{vmatrix} C_{\mathbf{g}}^j \\ C_{\mathbf{h}}^j \\ C_{\mathbf{l}}^j \end{vmatrix} = \mathbf{0}$$

or

$$HC = \mathbf{0}. \quad (3)$$

The condition for nontrivial solutions of (3) is

$$\text{Det } H = 0. \quad (4)$$

Equation (4) is the dispersion equation which determines the $E-k$ relation in the crystal and has $2n$ solutions where n is the total number of Fourier coefficients of the potential used. Using an xyz coordinate system, we define the coordinates such that the xy plane is parallel to the surface and the z axis inwards, in which case k_x and k_y are determined by

the boundary conditions (see below). Equations (3) and (4) can be solved using a quick eigenvalue searching method (e.g. Faddeeva, 1959) which gives $2nk_z$ values and the corresponding eigenvectors C_g .

The total electron wave inside the crystal can then be written as

$$\psi(\mathbf{r}) = \sum_j \epsilon^j \psi^j(\mathbf{r}) \quad (5)$$

where ϵ^j are the coefficients of the excited Bloch waves which, together with the reflection coefficients of the outgoing waves in vacuum, are determined by the boundary conditions.

3. Boundary conditions

The electron wave in the vacuum can be written

$$\begin{aligned} \Phi(\mathbf{r}) = & \exp(2\pi i \boldsymbol{\chi} \cdot \mathbf{r}) + R_0 \exp(2\pi i \mathbf{k}_0 \cdot \mathbf{r}) \\ & + \sum_g R_g \exp(2\pi i \mathbf{k}_g \cdot \mathbf{r}) \end{aligned} \quad (6)$$

where the first term is the incident wave, the second is the back-reflected or specular reflected wave and the third the back-diffracted waves with \mathbf{k}_0 and \mathbf{k}_g the wave vectors of the corresponding waves, and R_0 and R_g the reflected wave amplitudes. \mathbf{k}_0 and \mathbf{k}_g are related to the incident wave vector $\boldsymbol{\chi}$ by the following equations in the Laue case:

$$\mathbf{k}_0 = \boldsymbol{\chi} - 2\boldsymbol{\chi}_z \quad (7)$$

$$\begin{aligned} \mathbf{k}_g &= \boldsymbol{\chi} - 2\boldsymbol{\chi}_z + \mathbf{g} + \mathbf{s}_g \\ &= \mathbf{k}_0 + \mathbf{g} + \mathbf{s}_g \end{aligned} \quad (8)$$

where $\boldsymbol{\chi}_z$ is the projection of the incident wave vector on the surface normal (z axis), and \mathbf{s}_g is the excitation error which is taken along the z axis. Fig. 1 shows the coordination set up for our computational development in the Bragg case.

Considering energy conservation and conservation of the interfacial momentum on the boundary, we obtain

$$k_{0x} = \chi_x; \quad k_{0y} = \chi_y \quad (9)$$

$$k_{gx} = \chi_x - g_x; \quad k_{gy} = \chi_y - g_y \quad (10)$$

$$k_{0z} = -\chi_z \quad (11)$$

$$k_{gz} = -[\chi^2 - (\chi_x - g_x)^2 - (\chi_y - g_y)^2]^{1/2} \quad (12)$$

for the reflected waves, and

$$k_x^j = \chi_x; \quad k_y^j = \chi_y \quad (13)$$

for the Bloch waves. It should be noted that k_{gz} can be imaginary, if the value inside the square root is negative. This happens when the surface normal does not touch the dispersion sphere, which means that there exist evanescent waves in the outgoing wave which propagate along the surface but carry no energy. (Numerical results indicate that these external evanescent waves are quite common.)

Matching across the surface leads to the two sets of equations for the Bloch- and reflected-wave amplitudes:

$$\delta_{0g} + R_g = \sum_j \epsilon^j C_g^j \quad (14)$$

$$\delta_{0g} - R_g = \sum_j (k_z^j + g_z) \epsilon^j C_g^j / k_{gz} \quad (k_{gz} \neq 0). \quad (15)$$

There are apparently now $4n$ unknowns constrained by $2n$ boundary conditions, which is an insoluble problem. In order to solve this there are two approaches. One can use a slab model, invoking a second boundary parallel to the incoming surface of the crystal which will provide a further n boundary conditions as suggested by Moon (1972) and Colella (1972). Provided that the second surface is well separated from the first and that the crystal is absorbing this method will be perfectly valid. The second method, which has been briefly described in an earlier note (Marks & Ma, 1988a), is to use the current flow to obtain n boundary conditions. (We can use current

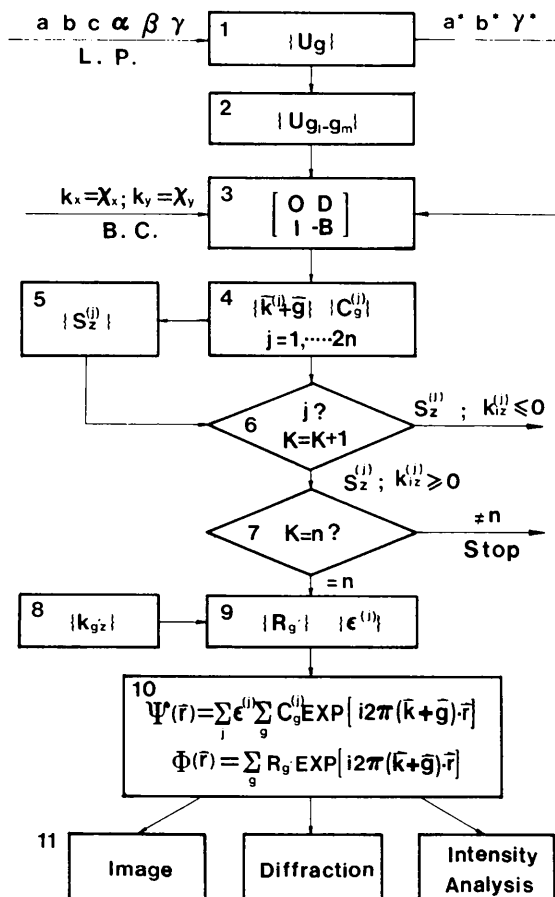


Fig. 1. An outline of the computer program for calculating the n -beam Bloch-wave solution in the Bragg case. a, b, c, α, β and γ are the unit-cell parameters, the matrices O, D, I and B are the same as those given by Metherell (1972) and the other terms are defined in the text.

Table 1. Listing of the Bloch waves for a nine-beam calculation of GaAs

The beam direction is along the (010) Laue zone axis tilted by 6.5 mrad along the [101] direction. For the absorption treatment, the imaginary parts of the Fourier potential coefficients are taken as 10% of their real parts. The upper part of the table compares the real and imaginary components of the wave vectors and current flow, the lower the excitation amplitudes.

Without absorption		With absorption	
Eigenvalues	Current flow	Eigenvalues	Current flow
1 (0.733, 0.000)	0.381	(0.733, 0.016)	0.381
2 (-0.733, 0.000)	-0.382	(-0.733, -0.016)	-0.383
3 (0.599, 0.000)	0.264	(0.601, 0.031)	0.265
4 (-0.599, 0.000)	-0.275	(-0.601, -0.031)	-0.276
5 (0.354, 0.149)	0.000	(0.378, 0.151)	0.021
6 (0.354, -0.149)	0.000	(0.330, -0.151)	-0.289
7 (-0.354, 0.149)	0.000	(-0.330, 0.151)	0.290
8 (0.245, 0.097)	0.000	(0.262, 0.092)	0.347
9 (0.245, -0.097)	0.000	(0.228, -0.107)	-0.055
10 (-0.354, -0.149)	0.000	(-0.378, -0.151)	-0.021
11 (-0.245, 0.097)	0.000	(-0.228, 0.107)	0.388
12 (-0.245, -0.097)	0.000	(-0.262, -0.092)	-0.087
13 (0.000, 0.149)	0.000	(0.024, 0.151)	0.260
14 (0.115, 0.054)	0.000	(0.145, 0.070)	0.909
15 (0.000, -0.149)	0.000	(-0.024, -0.151)	-0.024
16 (0.115, -0.054)	0.000	(0.086, -0.057)	-0.106
17 (-0.115, 0.054)	0.000	(-0.086, 0.057)	1.020
18 (-0.115, -0.054)	0.000	(-0.145, -0.070)	-0.070

Excitation amplitudes	
1	0.187×10^{-2}
3	0.538
5	0.125×10^{-10}
7	0.611×10^{-10}
8	0.655
11	0.0452
13	0.381×10^{-13}
14	0.180×10^{-2}
17	0.705×10^{-4}

flow, group velocity, probability flow or energy flow essentially interchangeably since these all differ only by a scalar term.) The point is that the probability current flow on the entrance surface $z=0$, which is parallel to the *real* component of the vector normal to the dispersion surface and is given by

$$S = \text{Real part of } (he/m) \sum_g |C_g^j|^2 (\mathbf{k}^j + \mathbf{g}), \quad (16)$$

determines the path of the energy carried by the electrons. The Bloch waves which physically exist in the crystal must satisfy $S_z > 0$ and k_z^j must have a non-negative imaginary component, these two conditions being in fact identical when absorption is included (Marks & Ma, 1988a). The two conditions eliminate n Bloch waves and therefore make the boundary condition problem soluble. [The generalized Hill's-determinant method suggested by Moon (1972) would appear to be equivalent, but substantially more complicated.]

The concept of current flow introduced here is one which goes beyond the boundary-value problem and is very useful in understanding the physics of reflection diffraction. Several points should be stressed.

Table 2. Values of \mathbf{g} ($g_y=0$), k_{gz} and the reflection coefficient $|R_g|$ for the example in Table 1

The strongly excited evanescent waves outside the surface should be noted.

	g_x	g_z	k_{gz}	$ R_g $
1	-0.3546	-0.3546	(0.0000, -0.3071)	0.441
2	-0.3546	0.0000	(0.0000, -0.3071)	0.00764
3	-0.3546	0.3546	(0.0000, -0.3071)	0.104
4	0.0000	-0.3546	(-0.1773, 0.0000)	0.0334
5	0.0000	0.0000	(-0.1773, 0.0000)	0.393
6	0.0000	0.3546	(-0.1773, 0.0000)	0.0024
7	0.3546	-0.3546	(0.0000, -0.3071)	0.441
8	0.3546	0.0000	(0.0000, -0.3071)	0.00764
9	0.3546	0.3546	(0.0000, -0.3071)	0.104

Firstly, k_z and S_z do not smoothly follow each other at all, and it is dangerous to use k_z to explain any physical phenomena since it would be misleading. As a concrete example, Table 1 shows numerical results for a GaAs (001) surface, illustrating the relationship between the signs of k_{gz} , k_{iz} and S_z both with and without absorption. Table 2 shows for the same example the wave vectors and reflection coefficients which indicate the role of external evanescent waves. It should also be appreciated that S_z depends upon the real part of the derivative of the dispersion surface, *i.e.* both the real and imaginary components play a role. Another important point is that S_z for the total reflected or transmitted wave is the (independent) sum of the different S_z contributions from the separate plane or Bloch waves. Finally, in the absence of absorption conservation of probability indicates that $\nabla \cdot \mathbf{S} = 0$ (Marks & Ma, 1988a). [It should be pointed out that this conservation of current flow can also be derived if we treat (14) and (15) as vector equations and take the dot product.] Therefore, if we monitor the current flow into the crystal, we are automatically monitoring the reflectivity. The importance of this will become apparent later when we consider the variations in wave vectors and current flow as a function of the incident-beam direction.

The unknowns can now be uniquely determined by writing in matrix form

$$\begin{pmatrix} C & -I \\ A & I \end{pmatrix} \begin{pmatrix} \varepsilon \\ R \end{pmatrix} = \begin{pmatrix} J \\ J \end{pmatrix} \quad (17)$$

where the matrices are

$$C = \begin{pmatrix} C_0^1 & C_0^2 & \dots & C_0^n \\ C_g^1 & C_g^2 & \dots & C_g^n \end{pmatrix} \quad (18)$$

$A =$

$$\begin{pmatrix} k_z^1 C_0^1 / k_{0z} & k_z^2 C_0^2 / k_{0z} & \dots & k_z^n C_0^n / k_{0z} \\ (k_z^1 + g_z) C_0^1 / k_{gz} & (k_z^2 + g_z) C_0^2 / k_{gz} & \dots & (k_z^n + g_z) C_0^n / k_{gz} \end{pmatrix} \quad (19)$$

with I the unit matrix and

$$\mathbf{J} = \begin{pmatrix} 1 \\ 0 \\ \vdots \\ 0 \end{pmatrix}, \quad (20)$$

so that

$$\boldsymbol{\varepsilon} = 2(\mathbf{C} + \mathbf{A})^{-1}\mathbf{J} \quad (21)$$

$$\mathbf{R} = \frac{1}{2}(\mathbf{C} - \mathbf{A})\boldsymbol{\varepsilon}. \quad (22)$$

4. Numerical development and results

To solve numerically (Fig. 1) we assume that the crystal is perfect and that the surface plane is exactly perpendicular to the plane of the Laue zone. To calculate the crystal potential we employed the relevant parts of a multislice simulation program used at Northwestern University. This potential was converted to give the $2n \times 2n$ matrix which was solved as indicated in § 2. For the eigenvalue searching, we used the general complex matrix *EISPACK* package which also gives the eigenvectors C_g . The z component of the energy flow of each Bloch wave is then evaluated to reduce the possible Bloch waves, as outlined in § 3. The excitation and reflection coeffi-

cients are then solved, using complex linear equation routines in the *LINPACK* program package. Finally, we can construct the total Bloch wave in the crystal and total reflected wave in the vacuum from all previous calculated parameters, writing the wave out in a form that the existing imaging routines originally written for multislice simulation can handle. Utilizing the constructed waves, we can either display ideal diffraction patterns and images or analyze the beam intensities and wave intensities. It should be mentioned that at this stage we discriminate between the evanescent waves outside the surface and the outgoing waves, so that we do not obtain artifacts from these evanescent waves.

Fig. 2 shows as an example results for intensity maps of both the reflection wave in vacuum and the Bloch wave in the crystal. These are shown over 5×5 unit cells, *i.e.* $28.2 \times 28.2 \text{ \AA}$. The incident energy is 100 keV and the incident glancing angle is 42 mrad. The beam is along the [010] azimuth. The diffraction pattern is a direct Fourier transform of the reflected wave and shows seven spots corresponding to 49 excited beams in the crystal forming a semicircle. Because the calculation is for a perfect surface, the reflected spots are sharp as dictated by momentum conservation.

5. Dynamical phenomena in Bragg reflection

In this section we will very briefly discuss some of the dynamical effects in reflection diffraction.

5.1. Surface resonance condition

Intensity enhancements of a particular diffraction spot have been extensively studied in LEED and RHEED. First noticed by Kikuchi & Nakagawa (1933) and more recently by Miyake, Kohra & Takagi (1954), McRae (1966), McRae & Caldwell (1967), Miyake & Hayakawa (1970), Ichimiya, Kambe & Lehmpfuhl (1980) and Marten & Meyer-Ehmsen (1985), the intensities of the specular and Bragg reflected spots are anomalously enhanced when the spot intersects a Kikuchi line. In particular Marten & Meyer-Ehmsen (1985) have suggested a method of understanding resonance in terms of surface bound states.

From a Bloch-wave viewpoint, there are in fact *two* different effects, both of which occur near to the resonant condition, which lead to various changes in the net reflectivity. These correspond to total internal reflection of Bloch waves or total external reflection of diffracted waves. It should be noted that for electrons a solid is polyrefractive since the S for each Bloch wave leads to a different refractive index, and we have n diffracted waves so we can expect a large number of internal/external reflection conditions. Analysis based solely upon total internal reflection

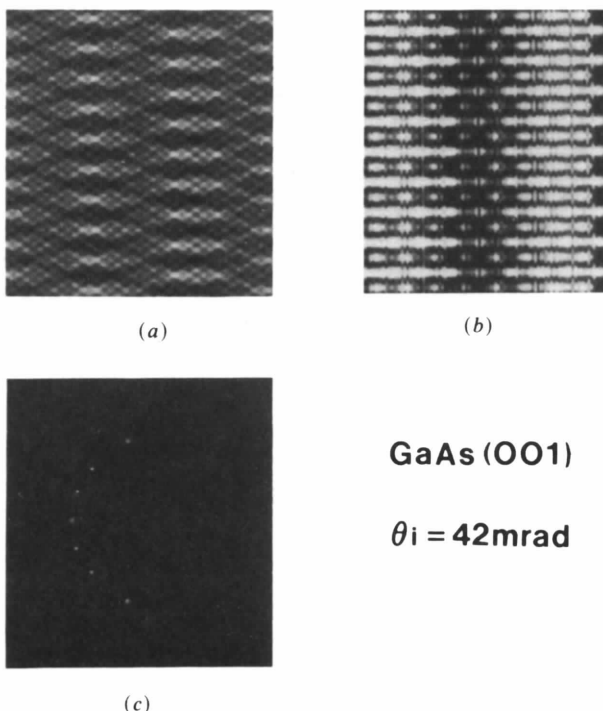


Fig. 2. Calculated results for GaAs (001) with the incident beam along the [010] azimuth with a tilt of 42 mrad for 100 keV electrons: (a) intensity map of reflected wave; (b) intensity map of the Bloch wave in the crystal; (c) diffraction pattern. External surface evanescent waves are not included in (c).

due to the mean inner potential is not adequate since refraction is determined by the behavior of S , not the wave vector. We will discuss the two effects with reference to Figs. 3-7 which show respectively the rocking curve for the reflected wave, the total reflectivity, the wave vector of some of the reflected waves and the real, imaginary and current flows of the three major Bloch waves, all for GaAs near to a [110] zone.

The first effect is total reflection of a particular diffracted wave, *i.e.* when the incident angle is varied a diffracted wave changes from an escaping plane wave to a trapped evanescent wave on the outside of the surface. This occurs when the condition $k_{gz} = 0$ is satisfied for the particular Bragg incident angle, consistent with the analysis of McRae (1966), McRae & Caldwell (1967) and Miyake & Hayakawa (1970), and can be seen by comparing Figs. 3, 4 and 5. There

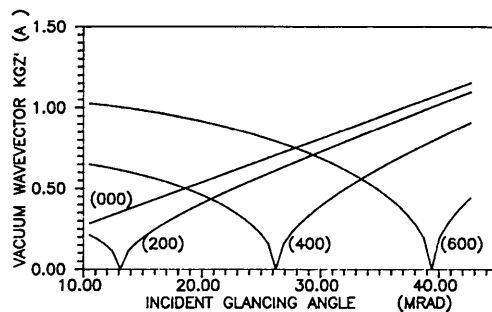


Fig. 5. Plots of the vacuum wave vectors as a function of incident angle. When the curves are decreasing the wave vector is purely imaginary, one of the resonance peaks is zero, and when the wave vector is increasing the value is fully real.

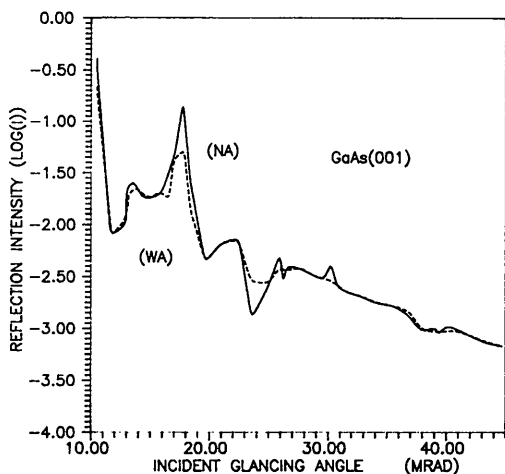


Fig. 3. Specular-beam rocking curves calculated for GaAs (001) surface with and without absorption for 100 keV and the (010) azimuth.

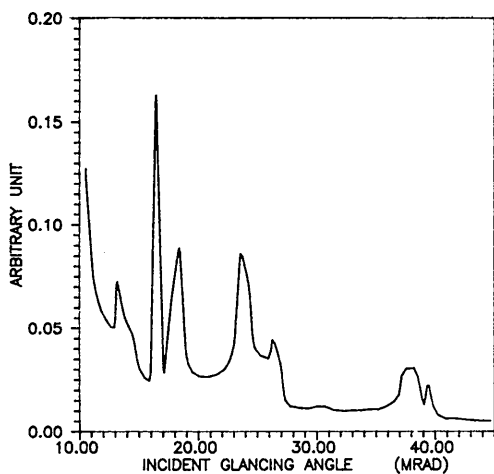
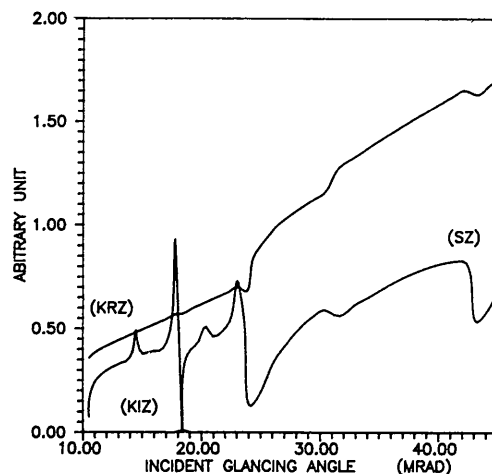
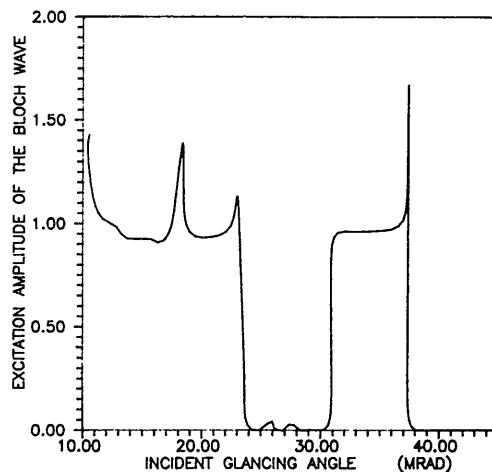


Fig. 4. Total reflectivity as a function of beam incidence angle for the same conditions as in Fig. 3.



(a)



(b)

Fig. 6. Plots for the strongest Bloch wave. (a) The real and imaginary components of the wave vector k , and k , respectively and the current flow S_z . (b) The excitation amplitude.

are peaks in both the specular reflected beam intensity and the total reflectivity at the condition where a reflected beam is transiting from evanescent to escaping, *i.e.* has a zero imaginary component, although these are not the strongest features in Figs. 3 and 4.

The second effect is when some of the Bloch waves within the crystal change from propagating into the crystal to being evanescent in character, *i.e.* total internal reflection of Bloch waves occurs. This occurs in the region where the normal to the Ewald sphere is lying in the 'band gap' between the Bloch-wave dispersion surfaces. Since an evanescent wave has $S_z = 0$, conservation of current indicates that this should lead to a maximum in the reflectivity. This can be seen by comparing Figs. 6 and 7 with the total reflectivity in Fig. 4, for instance the zero in the current flow in Fig. 6(a) at about 18.5 mrad and the corresponding peak in Fig. 4.

Although the above arguments provide some rationalization for the various peaks in the net reflectivity,

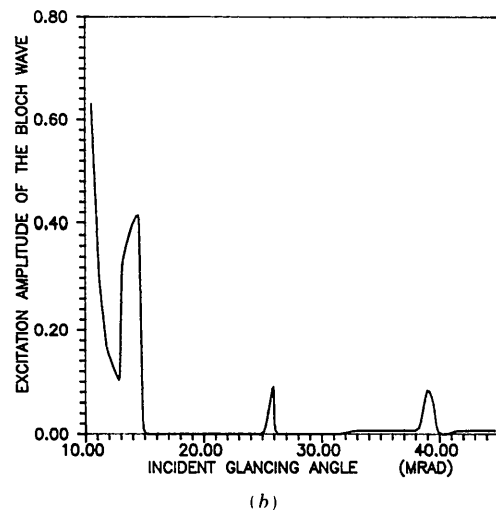
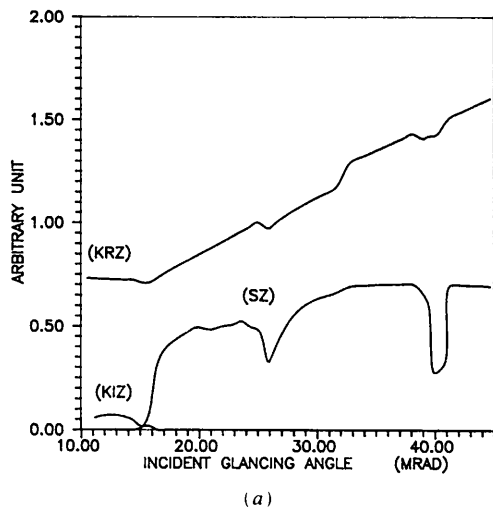


Fig. 7. As for Fig. 6, but for the next strongest Bloch wave.

they do not give a complete explanation. This indicates that the idea that total internal or external reflection is responsible for the intensity maxima, one which has been around in the literature for a long time, is not sufficient. It is apparent from the curves showing the excitations of the different Bloch waves as a function of angle that there are very large variations in these which are due to the boundary conditions rather than simply to changes in S arising from variations in the real and imaginary components of the wave vectors. For instance, the maximum in the total reflectivity at about 23.5 mrad correlates well with the zero excitation of the Bloch wave shown in Fig. 6(b). From this we would conclude that although resonance effects based upon total internal or external reflection are important, they do not explain all the intensity variations and many of these must be due to some combination of the boundary conditions and the changing character of the Bloch waves.

5.2. Splitting of Bragg spots

Equations (9)–(12) contain one interesting feature: the z component of the reflected wave vectors is completely independent of g_z . This means that the wave vectors of all the reflected plane waves generated by reciprocal-lattice points on a row perpendicular to the surface will overlap for a perfectly flat surface. The escaping diffracted beams form a semicircle consistent with experimental results, but each spot is actually the overlap (coherent sum) of a series of spots.

This initially strange result is the source of the phenomenon of Bragg spot splitting, first observed by Kikuchi & Nakagawa (1933). These authors showed that Bragg spots often split into two or more intensity maxima, depending on the azimuthal angle of the crystal. More recently, Pukite, Van Hove & Cohen (1984), Pukite & Cohen (1987) and Hsu & Cowley (1983) have shown that this splitting is consistent with a periodic array of steps.

If the surface deviates slightly from the normal to the Laue-zone plane due to surface steps, the surface normal will be slightly oblique to the Laue-zone plane. Therefore the row of reciprocal-lattice points is no

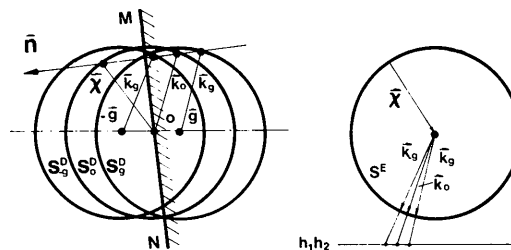


Fig. 8. Construction illustrating the dynamical origin of the splitting of the Bragg spots. MN is the surface, \mathbf{n} the surface normal and χ the incident wave vector.

longer normal to the surface, so the overlapped spots will split into a series of small spots. The mechanism is shown in Fig. 8. By simple geometry, it can be shown that the spot splitting is related to the beam direction with respect to the crystal lattice and surface normal and identical to the kinematical result. For reasons of space this analysis will be presented in more detail elsewhere (Marks & Ma, 1988*b*). It provides diffraction pattern details which are exact in terms of the positions of the spots (*e.g.* Pukite & Cohen, 1987) and show fairly good agreement in terms of the spot intensities.

As such, this spot splitting analysis is the dynamical equivalent of kinematical step spot splitting and the Bragg equivalent of wedge spot splitting in transmission (*e.g.* Cowley, 1981). However, it should be noted that this analysis also indicates that the width of a REM image of a step should vary linearly with the step separation (ignoring the effects of defocus and other imaging parameters). This appears to be in conflict with existing experimental results, and we therefore suspect that there must be additional contributions from strain fields around the steps at least when imaging well separated steps. This will be discussed in more detail elsewhere.

5.3. Extinction distance

The extinction distance is defined as the periodicity of the wave intensity oscillation in the crystal (Hirsch, Howie, Nicholson, Pashley & Whelan, 1977). Just as in transmission, the intensity oscillates as a function of depth within the crystal as shown in Fig. 9 for different incident angles and imaginary components

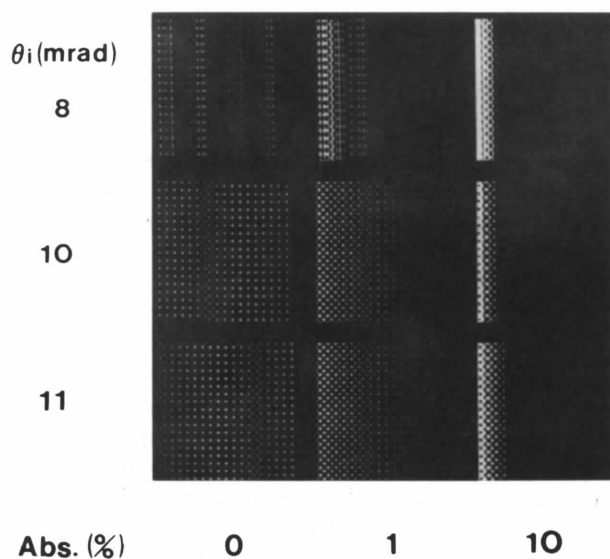


Fig. 9. Intensity maps for GaAs crystal at different incident glancing angles and with different absorption for 100 keV electrons and a (010) azimuth. The size of each picture is nine unit cells by nine unit cells, *i.e.* $50.57 \times 50.57 \text{ \AA}$.

to the potential for a GaAs (001) surface. The first column of images in Fig. 9 shows the results without absorption, the middle column with an imaginary component of 1% and the last column with a 10% component. As the imaginary component increases, the oscillations decay faster within the crystal, as would be expected, and the Bloch waves in the crystal have significant intensity only in the range of 10–15 Å for the 10% case. It should be noted that in the two-beam approximation we obtain an extinction distance of 12.64 Å, which is fairly close to the numerically calculated values. Similar oscillations can be found in some of the results of Peng & Cowley (1986), although it should also be pointed out that the intensity oscillations here have a fairly substantial period, not the smaller period observed by these authors.

6. Discussion

One feature of the Bragg solutions that differs from the more common Laue solutions is the central role of the current flow. As mentioned earlier, current flow is both additive and conserved across the entrance surface of the crystal, and is therefore a simple method of understanding the physics of the problem. It is also parallel to the real part of the gradient of the dispersion surface, which can be readily sketched, permitting qualitative understanding. Provided that we follow this approach, the Bragg solutions are not really all that different from the Laue solutions.

One feature that merits a little discussion is momentum conservation which in the Laue case for a perfect crystal leads only to semicircles of diffraction spots, not to the two-dimensional patterns which are experimentally found in many REM experiments. For a perfect crystal there is no mechanism for momentum transfer except normal to the surface or by reciprocal-lattice vectors in the plane of the surface. This can be seen from a simple kinematical argument if one considers the intersection of the Ewald sphere with the one-dimensional *rel*-rods normal to the crystal surface from each reciprocal-lattice spot. However, in real specimens the crystal is vibrating and there are inelastic excitations of both plasmons and phonons which can provide other momentum transfers. In a Bloch-wave model we can consider these as leading to vertical transitions, which indicates that phonons are the most likely source of two-dimensional diffraction since phonons lead to intra-branch scattering as is well established for small-angle scattering in transmission.

Some limits to the Bloch-wave method should also be mentioned, the most notable of which is for phenomena such as surface relaxations or reconstructions. Neither of these can be incorporated very conveniently into the Bloch-wave model. However, there are many well established Bloch-wave techniques

which can be used for defective structures, so it should be possible to use these for relaxations or reconstructions, as well as features such as surface steps. Another approach which we intend to exploit in the near future is to employ the Bloch-wave solutions as the incoming wave for a multislice calculation which should allow us to calculate very accurately diffraction effects at surface steps, for instance. Limitations of the Bloch-wave approach aside, it does yield substantial physics, for instance the explanation of step spot splitting described in § 5.2.

References

- BETHE, H. A. (1928). *Ann. Phys. (Leipzig)*, **87**, 55-129.
 COLELLA, R. (1972). *Acta Cryst.* **A28**, 11-15.
 COLELLA, R. & MENADUE, J. F. (1972). *Acta Cryst.* **A28**, 16-22.
 COWLEY, J. M. (1981). *Diffraction Physics*. Amsterdam: North-Holland.
 FADDEEVA, V. N. (1959). *Computational Methods of Linear Algebra*. New York: Dover.
 HIRSCH, P. B., HOWIE, A., NICHOLSON, R. B., PASHLEY, D. W. & WHELAN, M. J. (1977). *Electron Microscopy of Thin Crystals*. London: Butterworths.
 HSU, T. & COWLEY, J. M. (1983). *Ultramicroscopy*, **11**, 239-250.
 ICHIMIYA, A., KAMBE, K. & LEHMPPFUHL, G. (1980). *J. Phys. Soc. Jpn.*, **46**, 684-688.
 KIKUCHI, S. & NAKAGAWA, S. (1933). *Sci. Pap. Inst. Phys. Chem. Res. Tokyo*, **21**, 256-265.
 MA, Y. & MARKS, L. D. (1989). In preparation.
 MAKSYM, P. A. & BEEBY, J. L. (1981). *Surf. Sci.* **110**, 423-438.
 MARKS, L. D. & MA, Y. (1988a). *Acta Cryst.* **A44**, 392-393.
 MARKS, L. D. & MA, Y. (1988b). Submitted to *Surf. Sci.*
 MARTEN, H. & MEYER-EHMSEN, G. (1985). *Surf. Sci.* **151**, 570-584.
 MCRAE, E. G. (1966). *J. Chem. Phys.* **45**, 3258-3276.
 MCRAE, E. G. & CALDWELL, C. W. (1967). *Surf. Sci.* **7**, 41-67.
 MENADUE, J. F. (1972). *Acta Cryst.* **A28**, 1-11.
 METHERELL, A. J. (1972). *Electron Microscopy in Materials Science*, edited by U. VALDRE & E. RUEDL, Vol. II, pp. 397-552. Brussels: Commission of the European Communities.
 MIYAKE, S. & HAYAKAWA, K. (1970). *Acta Cryst.* **A26**, 60-70.
 MIYAKE, S., KOHRA, K. & TAKAGI, M. (1954). *Acta Cryst.* **7**, 393-401.
 MOON, A. R. (1972). *Z. Naturforsch. Teil A*, **27**, 390-395.
 PENG, L.-M. & COWLEY, J. M. (1986). *Acta Cryst.* **A42**, 545-552.
 PUKITE, P. R. & COHEN, P. I. (1987). *Appl. Phys. Lett.* **50**, 1739-1741.
 PUKITE, P. R., VAN HOVE, J. M. & COHEN, P. I. (1984). *Appl. Phys. Lett.* **44**, 456-458.
 SCHUMAN, H. (1977). *Ultramicroscopy*, **2**, 261-269.

Acta Cryst. (1989). **A45**, 182-187

Direct Determination of Triplet Phases and Enantiomorphs of Non-centrosymmetric Structures. II. Experimental Results

BY K. HÜMMER, E. WECKERT AND H. BONDZA

Institut für Angewandte Physik, Lehrstuhl für Kristallographie der Universität, Bismarckstrasse 10, D-8520 Erlangen, Federal Republic of Germany

(Received 19 April 1988; accepted 19 September 1988)

Dedicated to Ulrich Bonse on the occasion of his 60th birthday

Abstract

Direct measurements of triplet phase relationships for non-centrosymmetric light-atom organic structures with medium-size unit cells are reported. The phase information can be extracted from the three-beam profiles of a Renninger ψ -scan experiment. The measurements were carried out with a special ψ -circle diffractometer installed on a rotating Cu-anode generator. The incident-beam divergence is reduced to 0.02° . The experimental results confirm the theoretical considerations of paper I of this work [Hümmer & Billy (1986). *Acta Cryst.* **A42**, 127-133]. As triplet phases of $\pm 90^\circ$ can be distinguished, the absolute structure can be determined unambiguously. The measurements show that the triplet-phase-dependent interference effects may be superposed on phase-independent *Umweganregung* or *Aufhellung* effects. By a comparison of the ψ -scan profiles of two cen-

trosymmetrically related three-beam cases, the triplet phases of which have opposite signs, it is possible to evaluate the phase-independent effects and to determine the value of the triplet phase with an accuracy of at least 90° .

1. Introduction

In paper I of this work (Hümmer & Billy, 1986) the use of ψ -scan profiles near a three-beam case for the experimental determination of structure-invariant triplet phase sums was discussed in particular for non-centrosymmetric crystal structures. The idea of exploiting the three-beam interference to obtain information on the X-ray reflection phases is based on the fact that in an interference experiment the resultant amplitude depends not only on the amplitudes of the interfering waves but also on their phase difference (Lipscomb, 1949; Post, 1977).